



Static and dynamic structure of ZnWO₄ nanoparticles

A. Kalinko*, A. Kuzmin

Institute of Solid State Physics, University of Latvia, Kengaraga Street 8, LV-1063 Riga, Latvia

ARTICLE INFO

Article history:

Received 14 September 2010
Received in revised form 10 February 2011
Accepted 12 February 2011
Available online 16 March 2011

Keywords:

ZnWO₄;
Nanoparticles;
Zn K-edge;
W L₃-edge;
EXAFS;
X-ray diffraction;
Raman spectroscopy;
Photoluminescence

ABSTRACT

Static and dynamic structure of ZnWO₄ nanoparticles, synthesized by co-precipitation technique, has been studied by temperature dependent x-ray absorption spectroscopy at the Zn K-edge and W L₃-edge. Complementary experimental techniques, such as x-ray powder diffraction, Raman and photoluminescence spectroscopies, have been used to understand the variation of vibrational, optical, and structural properties of nanoparticles, compared to microcrystalline ZnWO₄. Our results indicate that the structure of nanoparticles experiences strong relaxation leading to the significant distortions of the WO₆ and ZnO₆ octahedra, being responsible for the changes in optical and vibrational properties.

© 2011 Elsevier B.V. All rights reserved.

1. Introduction

Tungstates having general formula A²⁺WO₄ are extremely interesting compounds, which find many practical applications as scintillators [1–3], optical fibers [4], solid state Raman lasers [5,6], catalysts [7], high-temperature solid lubricants [8], gas sensors [9], and phase-change optical memories [10]. Among them wolframite-type ZnWO₄, also known as mineral sanmartinite, has attracted recently a considerable interest both from experimental and theoretical points of view [11–14] due to optical and catalytic properties as well as possibility of preparation in nanosized [9,15] and thin film forms [10,16,17].

It is known that the structure of nanomaterials experiences a relaxation (either contraction or expansion) compared to their bulk counterpart, leading to a size-induced property change [18,19]. Thus, the knowledge of the relaxation processes is crucial for understanding and tailoring of nanomaterial properties, however their detailed studies still remain a challenge [20]. The problem with probing atomic structure at the nanoscale is mainly related to limitations induced by experimental methods, therefore the use of several complementary techniques is an advantage.

In this work we have applied x-ray absorption spectroscopy at the Zn K-edge and W L₃-edge to probe the local structure and its temperature dependence in ZnWO₄ nanoparticles in comparison with microcrystalline compound. The complementary use of the experi-

mental techniques, such as x-ray powder diffraction, Raman and photoluminescence spectroscopies, allowed us to construct a nanoparticle model consistent with their structural, vibrational, and optical properties.

2. Experimental details

ZnWO₄ nanoparticles were synthesized using co-precipitation technique [7,21] by the reaction of ZnSO₄ · 7H₂O and Na₂WO₄ · H₂O at room temperature (20 °C), pH = 8, and reaction time 1–2 h. All chemicals used were of analytic grade reagents (purity 99%, “Reahim”) without further purification. The water solutions of the two salts were prepared by dissolving 10 mmol of the salt in 100 ml of double-distilled water with vigorous stirring. Next they were mixed in 1:1 molar ratio, and white precipitates appeared immediately. After completion of the reaction, the precipitate was filtered off, washed several times with double-distilled water, and dried in air for 12 h at 80 °C thus resulting in the white-colored nanocrystalline ZnWO₄ powder. The microcrystalline ZnWO₄ powder was also produced to use for comparison by annealing nanocrystalline powder in air for 4 h at 800 °C. Thus all powders obtained were white-colored.

The samples were characterized at room temperature (20 °C) by x-ray powder diffraction, Raman and photoluminescence spectroscopies [21].

X-ray absorption measurements were performed in transmission mode at the HASYLAB DESY C1 bending-magnet beamline in the temperature range from 10 K to 300 K at the Zn K (9659 eV) and W L₃ (10,207 eV) edges. The storage ring DORIS III operated at $E = 4.44$ GeV and $I_{\text{max}} = 140$ mA. The x-ray beam intensity was measured by two

* Corresponding author.

E-mail address: akalin@latnet.lv (A. Kalinko).

URL: <http://www.cfi.lv/> (A. Kalinko).

ionization chambers filled with argon and krypton gases. The higher-order harmonics were effectively eliminated by detuning of the double-crystal monochromator Si(111) to 60% of the rocking curve maximum, using the beam-stabilization feedback control. The Oxford Instruments liquid helium flow cryostat was used to maintain the required sample temperature. The temperature was stabilized to within ± 0.5 K during each experiment. The powder samples were deposited on Millipore filters and fixed by Scotch tape. The deposited powder weight was chosen to give the value of the absorption jump close to 1.0 at both Zn K and W L_3 edges. The two edges were measured using scans over long energy interval from 9500 eV to 11,300 eV (Fig. 1).

3. EXAFS data analysis

X-ray absorption spectra at the Zn K-edge and W L_3 -edge (Fig. 1) were analyzed using the EDA software package [22]. The EXAFS signals $\chi(k)$ were defined as

$$\chi(k) = \left[\mu_{\text{exp}}(E) - \mu_0(E) - \mu_b(E) \right] / \mu_0(E) \quad (1)$$

where $\mu_{\text{exp}}(E)$ is the experimental absorption coefficient, $\mu_b(E)$ is the pre-edge background extrapolated beyond the absorption edge, $\mu_0(E)$ is the atomic-like contribution, $k = [(2m_e/\hbar^2)(E - E_0)]^{1/2}$ is the wave vector, and E_0 is the photoelectron energy origin. The E_0 position in the experimental signals was set at 10,210 eV for W L_3 -edge and at 9664 eV for Zn K-edge to have the best match between k -space scales of the experimental and theoretical, calculated by the FEFF8.2 code [23], EXAFS signals.

The experimental EXAFS $\chi(k)k^2$ signals and their Fourier transforms (FT) at selected temperatures are shown in Figs. 2 and 3, respectively. Their shapes are close in the whole temperature range, however the EXAFS signals intensity and the FT peaks amplitude decrease upon increasing temperature due to the thermal damping effect. The same 10% Gaussian window was used in FT and back-FT transformations. Note that the positions of the FT peaks are shifted in Fig. 3 from their true crystallographic values because the FTs were calculated without phase shift corrections. In this work only the first coordination shell contributions, singled out by the back-FT procedure in the range of ≈ 0.8 – 2.4 Å, are considered.

To extract structural information, the first shell EXAFS $\chi(k)k^2$ signals were best-fitted using a model-independent approach [24] allowing the reconstruction of the true radial distribution function (RDF) $G(R)$

$$\chi(k) = \int_{R_{\text{min}}}^{R_{\text{max}}} \frac{G(R)}{kR^2} F(\pi, k, R) \sin(2kR + \Phi(\pi, k, R)) dR, \quad (2)$$

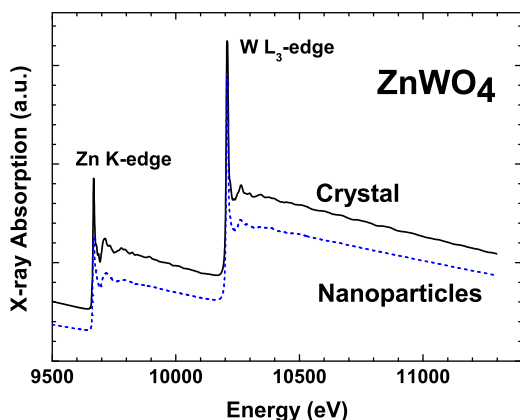


Fig. 1. X-ray absorption spectra in nanoparticles (dashed line) and microcrystalline (solid line) ZnWO₄ at 10 K. The two edges (Zn K and W L_3) are separated by 550 eV.

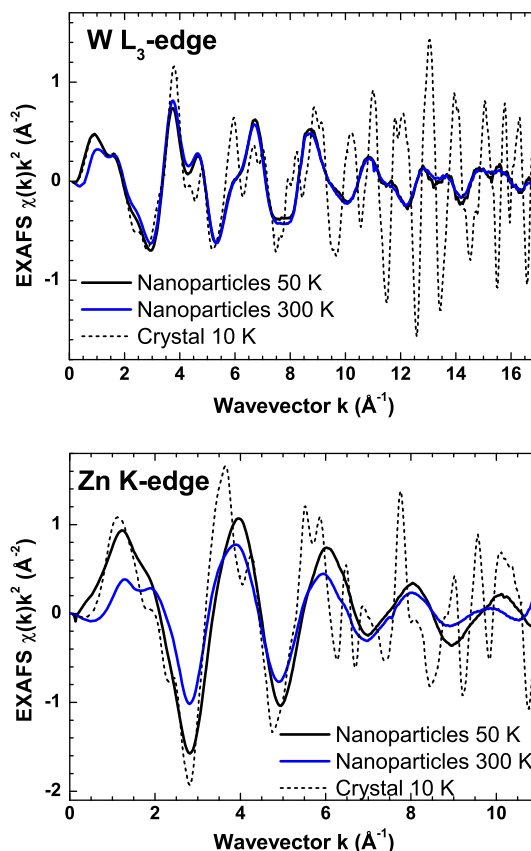


Fig. 2. Experimental W L_3 -edge and Zn K-edge EXAFS spectra from nanoparticles and microcrystalline ZnWO₄. Only representative signals are shown for clarity.

where $F(\pi, k, R)$ is the scattering amplitude function and $\Phi(\pi, k, R)$ is the phase shift function. The scattering amplitude (F) and phase shift (Φ) functions for W–O and Zn–O atom pairs were calculated by ab initio multiple-scattering code FEFF8.2 [23] using the complex exchange–correlation Hedin–Lundqvist potential. The calculations were performed based on the crystallographic structure of ZnWO₄ [13,25,26], considering a cluster of 8 Å size around the absorbing atom (W or Zn). Calculations of the cluster potentials were done in the muffin-tin (MT) self-consistent-field approximation using default values of MT radii as provided within the FEFF8.2 code [23].

The best-fits were performed in the k -space ranges of 1.5 – 16 Å⁻¹ at the W L_3 -edge and 1.5 – 10.5 Å⁻¹ at the Zn K-edge. The k -space range at the Zn K-edge is shorter due to the close presence of the W L_3 -edge (Fig. 1). The results of the best-fits and corresponding RDFs are shown in Figs. 4 and 5. Note very good agreement between the experimental and theoretical first shell EXAFS signals in Fig. 4, and significant difference between distortions of the WO₆ and ZnO₆ octahedra in nanoparticles and microcrystalline ZnWO₄ (Fig. 5). Finally, the obtained RDFs were decomposed into a set of Gaussian functions depending on the three structural parameters (the coordination number N , the interatomic distance R and the mean-square relative displacement σ^2), which are reported in Table 1.

4. Results and discussion

Crystalline ZnWO₄ has monoclinic ($P2_1/c$) wolframite-type structure built up of distorted WO₆ and ZnO₆ octahedra joined by edges into infinite zigzag chains, consisting of octahedral units of the same type and running parallel to c -axis [13,25,26]. The octahedra distortion results in the splitting of the W–O and Zn–O distances into three groups with the bond lengths of 1.790, 1.905, and 2.130 Å for tungsten atoms and 2.023, 2.086, and 2.217 Å for zinc atoms

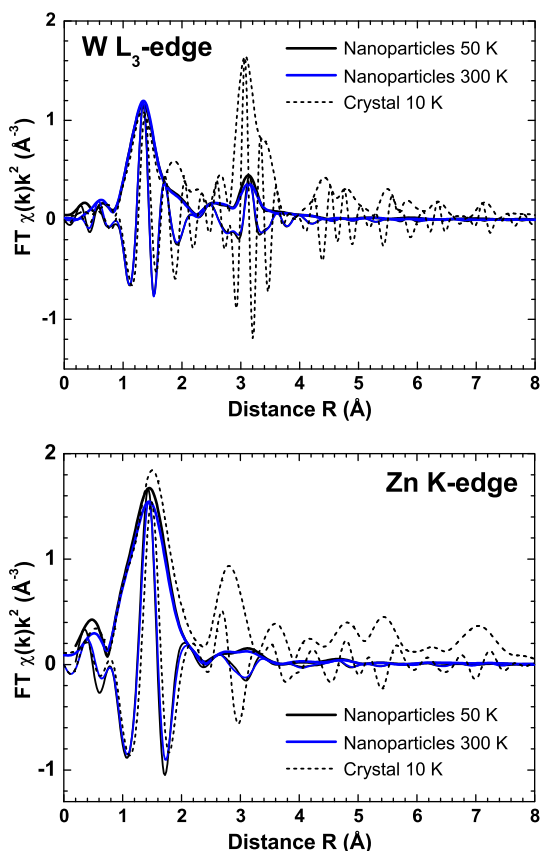


Fig. 3. Fourier transforms (FT) of the experimental W L_3 -edge and Zn K-edge EXAFS spectra from nanoparticles and microcrystalline $ZnWO_4$. Both modulus and imaginary parts are shown. Only representative signals are shown for clarity.

[13,25,26]. Our XRD measurements [21] confirm the wolframite-type of microcrystalline $ZnWO_4$, whereas no Bragg peaks appear in the XRD pattern for nanoparticles, indicating that the nanoparticles size is below 2 nm.

The vibrational properties of nanoparticles and microcrystalline $ZnWO_4$ were studied by us recently using Raman spectroscopy, which is sensitive to local vibrations and, thus, is perfectly suitable for nanoparticles studies [27].

In microcrystalline $ZnWO_4$, the group theory analysis predicts 36 lattice modes, of which 18 even vibrations ($8A_g + 10B_g$) are Raman active [28,29]. Only eleven of them (907, 787, 709, 679, 547, 516, 409, 355, 343, 315, and 276 cm^{-1}) are observed in the frequency range accessible in our experimental setup [21] due to the cut-off by the edge filter around 270 cm^{-1} . The highest mode at 907 cm^{-1} with a full width at half maximum (FWHM) of about 9 cm^{-1} corresponds to the stretching W–O vibrations [28,29]. The Raman signal changes drastically in nanoparticles. Here only the highest mode survives, but shifts to higher frequencies ($950\text{--}960\text{ cm}^{-1}$), and the band becomes broadened (FWHM = 50 cm^{-1}). We attribute the band broadening to the tungsten site and nanoparticles size distributions, whereas the position of the band is typical for the double tungsten–oxygen bonds [30] and can be related to the presence of the W=O bonds at the nanoparticle surface.

Luminescent properties of nanoparticles also differ from that observed in microcrystalline material [21]. The luminescence band at 2.55 eV in microcrystalline $ZnWO_4$ has a complex shape being similar to that in Ref. [31]: it envelops three emission bands, namely yellow at 2.28 eV, green at 2.51 eV, and blue at 2.80 eV [21]. The green–blue luminescence is believed to be due to radiation transitions of the charge transfer type between oxygen and tungstate states in regular octahedral WO_6 groups [2,32–34], while yellow luminescence was

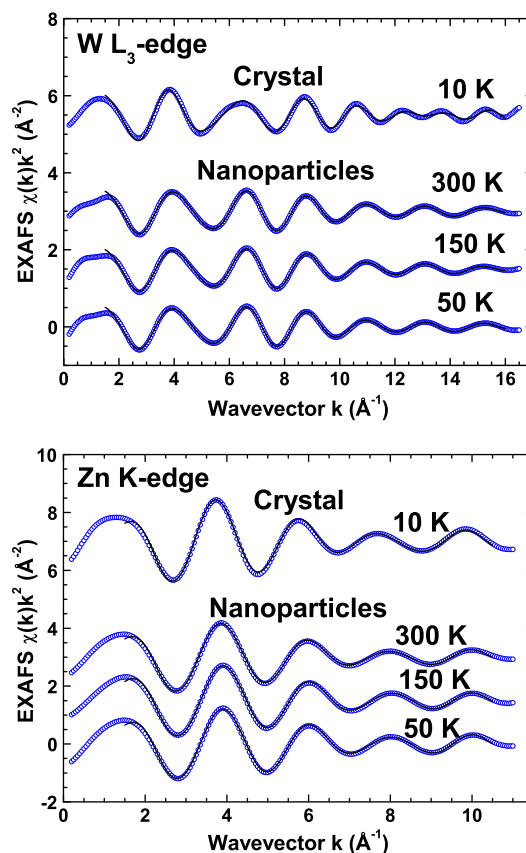


Fig. 4. Best fits (solid lines) of the first coordination shell experimental (open circles) W L_3 -edge and Zn K-edge EXAFS signals from nanoparticles and microcrystalline $ZnWO_4$ at different temperatures.

tentatively attribute to defective tungsten groups lacking one oxygen atom [16].

In nanoparticles, the maximum of the luminescence band experiences a red shift by 0.15 eV, and the complex shape of the band becomes more evident: it can be decomposed into three sub-bands peaked at 2.14 eV, 2.40 eV, and 2.69 eV [21]. The red shift of the band allows the exclusion of the presence of the quantum size effect, which should cause, on the contrary, a blue shift. The luminescence decay kinetics in nanoparticles is faster than in microcrystalline $ZnWO_4$ [21] and cannot be described by three component exponential decay, associated with the three types of self-trapped excitons [34], opposite to the case of microcrystalline [21,26] or single-crystal [35] $ZnWO_4$. The shift of the luminescence band position to lower energies and the acceleration of the luminescence kinetics can be explained by a significant deformation of WO_6 octahedra and by an influence of surface defects in nanoparticles. A simple estimate suggests that by taking the approximate size of the WO_6 or ZnO_6 octahedra being about twice the metal–oxygen bond, i.e. $\sim 4\text{ Å}$, the nanoparticle with a size of 2 nm will consist of less than 125 octahedral units, most (80%) of which will be located at the surface. As a result, the relaxation of the structure is inevitable leading to the decrease of the band gap and to appearance of defect centers able to trap excitons with different lifetimes. Such picture agrees well with the Raman results, discussed above, and with the results of our recent studies of the excitation spectrum in nanosized $ZnWO_4$ [36], which indicate a decrease of the optical band gap.

Thus, the direct proof of the metal–oxygen octahedra distortion in nanoparticles is required to provide a solid basis for the above-mentioned explanations. This information was obtained by x-ray absorption spectroscopy independently for W and Zn environments. Moreover, the temperature dependent EXAFS study allowed us to separate the static and thermal disorder contributions.

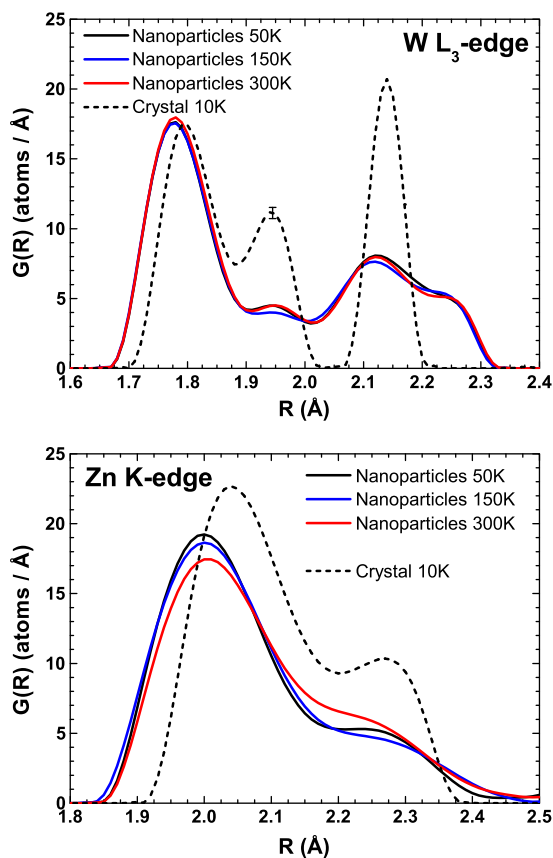


Fig. 5. The reconstructed RDFs $G(R)$ for the first coordination shell of tungsten and zinc in nanoparticles and microcrystalline ZnWO_4 at representative temperatures. See text for details.

The temperature dependent W L_3 -edge and Zn K-edge EXAFS spectra in nanoparticles and microcrystalline ZnWO_4 are shown in Fig. 2. The EXAFS signals for nanoparticles show weak temperature dependence and do not contain high-frequency contributions that indicates the absence of long-range order. In fact, the Fourier transforms of the EXAFS spectra, shown in Fig. 3, support this conclusion. While in microcrystalline ZnWO_4 the structural peaks are well visible up to 8 Å, the ordered region in nanoparticles is limited by about 4 Å.

The first coordination shell contribution from the nearest oxygen atoms gives a strong peak at 0.8–2.4 Å and is comparable in both nanoparticles and microcrystalline ZnWO_4 . However, already the second peak at ≈ 3 Å, being due to contributions from outer shells and multiple-scattering effects generated within the first shell, is strongly damped in nanoparticles. Further we analyze and discuss only the first coordination shell contribution.

Table 1

Parameters ($N (\pm 0.2)$, $R (\pm 0.02 \text{ \AA})$, $\sigma^2 (\pm 0.0005 \text{ \AA}^2)$) of the Gaussian functions obtained by the decomposition of the RDFs $G(R)$ in Fig. 5.

First shell W–O RDF $G(R)$ decomposition into the Gaussians													
	T (K)	N_1	R_1 (Å)	σ_1^2 (Å ²)	N_2	R_2 (Å)	σ_2^2 (Å ²)	N_3	R_3 (Å)	σ_3^2 (Å ²)	N_4	R_4 (Å)	σ_4^2 (Å ²)
Nanoparticles	50	2.7	1.78	0.002	1.2	1.92	0.006	1.6	2.13	0.004	0.5	2.25	0.001
Nanoparticles	150	2.7	1.78	0.002	1.1	1.91	0.007	1.7	2.13	0.004	0.4	2.25	0.001
Nanoparticles	300	2.8	1.78	0.002	1.2	1.93	0.007	1.5	2.13	0.003	0.5	2.25	0.001
Crystal	10	2.5	1.80	0.002	1.5	1.94	0.002	2.0	2.14	0.001			
First shell Zn–O RDF $G(R)$ decomposition into the Gaussians													
	T (K)	N_1	R_1 (Å)	σ_1^2 (Å ²)	N_2	R_2 (Å)	σ_2^2 (Å ²)						
Nanoparticles	50	3.7	2.00	0.005	1.7	2.20	0.012						
Nanoparticles	150	3.7	2.00	0.005	2.0	2.20	0.016						
Nanoparticles	300	3.0	2.00	0.005	2.3	2.18	0.014						
Crystal	10	4.0	2.05	0.004	2.0	2.24	0.005						

First, we have tried to analyze the first shell EXAFS signals using the conventional method, based on the multi-component fitting procedure within the Gaussian/cumulant approximations. However, the fitting procedure did not give good results, especially, in the case of nanoparticles. This indicates on the complex shape of the atomic distributions, in particular, strong distortion of the first shell octahedra. Therefore, a model-independent approach [24] allowing the reconstruction of the true RDF $G(R)$ was used.

The best-fit results are shown in Fig. 4. Very good agreement between experimental and calculated EXAFS $\chi(k)k^2$ signals was obtained at both W L_3 and Zn K edges. The simulated RDFs $G(R)$ at selected temperatures are shown in Fig. 5.

The RDF for microcrystalline ZnWO_4 corresponds well to the crystallographic structure [13,25,26], which assumes the existence of three groups of W–O bonds ($2 \times 1.79 \text{ \AA}$, $2 \times 1.91 \text{ \AA}$, and $2 \times 2.13 \text{ \AA}$) and Zn–O bonds (at $2 \times 2.03 \text{ \AA}$, $2 \times 2.09 \text{ \AA}$, and $2 \times 2.23 \text{ \AA}$). In fact, the strong distortion of the WO_6 octahedra in microcrystalline ZnWO_4 results in the three distinct peaks, located at 1.80 Å, 1.94 Å and 2.14 Å (see dashed line in Fig. 5 and Table 1). The local environment of zinc is also distorted, however, the first two groups of totally four oxygen atoms in ZnO_6 octahedra are located at close distances and, thus, contribute into the single broad peak at 2.05 Å, whereas the last group of two oxygen atoms contributes into the peak at 2.24 Å (see dashed line in Fig. 5 and Table 1).

The RDFs in nanoparticles are broadened compared to microcrystalline ZnWO_4 , especially at large distances, whereas the first peak is well defined and shifts to shorter distances (Fig. 5). This means that both tungsten and zinc atoms make stronger bonds with nearest oxygen atoms, whereas remaining oxygen atoms become weakly bound. The RDFs in nanoparticles show only minor temperature changes, especially around tungsten: this indicates that static disorder dominates the thermal one. Note that both octahedra distortion and nanoparticle distribution contribute into this effect.

The comparison of the RDFs around tungsten and zinc atoms suggests that the shortest W–O bonds are stronger, being more covalent [14], than the Zn–O bonds. The average coordination of both tungsten and zinc atoms remains always close to octahedral (Table 1) taking into account the error of the fit. The slightly smaller value of the total coordination number (5.3–5.7 atoms) for zinc atoms in nanoparticles can be related to the larger correlation between N and σ^2 parameters during the fit due to the shorter Zn K-edge EXAFS signal k -range (Fig. 4). Thus the behavior of the RDFs confirms strong distortion of the WO_6 and ZnO_6 octahedra in nanoparticles and is also favorable to the formation of the short W=O bonds, observed in the Raman spectrum [21].

5. Conclusions

Nanoparticles and microcrystalline ZnWO_4 were studied by temperature dependent x-ray absorption spectroscopy at the Zn K

and $W L_3$ edges. The obtained results were compared with that determined by complementary experimental techniques as x-ray powder diffraction, Raman and photoluminescence spectroscopies allowing us to probe different aspects of local atomic and electronic structures.

We have found that observed changes in the optical properties and lattice dynamics of nanoparticles cannot be attributed only to the size reduction, but are related to the relaxation of their atomic structure, including formation of surface defects.

The presence of strong structural relaxation was confirmed by x-ray absorption spectroscopy study. The independent analysis of the EXAFS signals at the $W L_3$ and $Zn K$ edges by model-independent approach [24] allowed us to reconstruct the first coordination shell RDFs and to follow their temperature dependencies. The significant distortions of the WO_6 and ZnO_6 octahedra, directly observed in nanoparticles by EXAFS, show only minor temperature dependence. The distortion results in the shortening of metal–oxygen bonds to the nearest oxygen atoms, whereas the longest bonds becomes weaker.

Acknowledgments

The authors are grateful to Dr. Dariusz A. Zajac at DESY for assistance during EXAFS measurements. This work was supported by the ESF Project 2009/0202/1DP/1.1.1.2.0/09/APIA/VIAA/141 and Latvian Government Research Grant No. 09.1518, and Latvian National Research Program IMIS. The research leading to these results has received funding from the European Community's Seventh Framework Programme (FP7/2007–2013) under grant agreement No. 226716 (Project I-20090071 EC).

References

- [1] T. Oi, K. Takagi, T. Fukazawa, *Appl. Phys. Lett.* 36 (1980) 278.
- [2] V.N. Kolobanov, I.A. Kamenskikh, V.V. Mikhailin, I.N. Shpinkov, D.A. Spassky, B.I. Zadneprovsky, L.I. Potkin, G. Zimmerer, *Nucl. Instrum. Methods Phys. Res. A* 486 (2002) 496.
- [3] H. Kraus, V.B. Mikhailik, Y. Ramachers, D. Day, K.B. Hutton, J. Telfer, *Phys. Lett. B* 610 (2005) 37.
- [4] H. Grassmann, H. Moser, E. Lorenz, *J. Lumin.* 33 (1985) 21.
- [5] J. Hulliger, A.A. Kaminskii, H.J. Eichler, *Adv. Funct. Mater.* 11 (2001) 243.
- [6] H.M. Pask, *Prog. Quantum Electron.* 27 (2003) 3.
- [7] G. Huang, Y. Zhu, *Mater. Sci. Eng. B* 139 (2007) 201.
- [8] S. Walck, J. Zabinski, N. McDevitt, J. Bultman, *Thin Solid Films* 305 (1997) 130.
- [9] X. Cao, W. Wu, N. Chen, Y. Peng, Y. Liu, *Sens. Actuators, B Chem.* 137 (2009) 83.
- [10] A. Kuzmin, R. Kalendarev, A. Kursitis, J. Purans, *J. Non-Cryst. Solids* 353 (2007) 1840.
- [11] D. Errandonea, F.J. Manjón, N. Garro, P. Rodríguez-Hernández, S. Radescu, A. Mujica, A. Muñoz, C.Y. Tu, *Phys. Rev. B* 78 (2008) 054116.
- [12] D. Errandonea, J. Pellicer-Porres, F.J. Manjón, A. Segura, C. Ferrer-Roca, R.S. Kumar, O. Tschauer, P. Rodríguez-Hernández, J. López-Solano, S. Radescu, A. Mujica, A. Muñoz, G. Aquilanti, *Phys. Rev. B* 72 (2005) 174106.
- [13] D.M. Trots, A. Senyshyn, L. Vasylechko, R. Niewa, T. Vad, V.B. Mikhailik, H. Kraus, *J. Phys. Condens. Matter* 21 (2009) 325402.
- [14] A. Kalinko, A. Kuzmin, R. Evarestov, *Solid State Commun.* 149 (2009) 425.
- [15] S.H. Yu, B. Liu, M.S. Mo, J.H. Huang, X.M. Liu, Y.T. Qian, *Adv. Funct. Mater.* 13 (2003) 639.
- [16] Z. Lou, J. Hao, M. Cocivera, *J. Lumin.* 99 (2002) 349.
- [17] X. Zhao, W. Yao, Y. Wu, S. Zhang, H. Yang, Y. Zhu, *J. Solid State Chem.* 179 (2006) 2562.
- [18] M. Fukuhara, *Phys. Lett. A* 313 (2003) 427.
- [19] C.Q. Sun, *Prog. Solid State Chem.* 35 (2007) 1.
- [20] S.J.L. Billinge, I. Levin, *Science* 316 (2007) 561.
- [21] A. Kalinko, A. Kuzmin, *J. Lumin.* 129 (2009) 1144.
- [22] A. Kuzmin, *Phys. B* 208–209 (1995) 175.
- [23] J.J. Rehr, R.C. Albers, *Rev. Mod. Phys.* 72 (2000) 621.
- [24] A. Kuzmin, J. Purans, *J. Phys. Condens. Matter* 12 (2000) 1959.
- [25] P.F. Schofield, K.S. Knight, G. Cressey, *J. Mater. Sci. A* 31 (1996) 2873.
- [26] H. Kraus, V.B. Mikhailik, L. Vasylechko, D. Day, K.B. Hutton, J. Telfer, Y. Prots, *Phys. Status Solidi* 204 (2007) 730.
- [27] G. Gouadec, P. Colombany, *Prog. Cryst. Growth Charact. Mater.* 53 (2007) 1.
- [28] Y. Liu, H. Wang, G. Chen, Y.D. Zhou, B.Y. Gu, B.Q. Hu, *J. Appl. Phys.* 64 (1988) 4651.
- [29] H. Wang, F.D. Medina, Y.D. Zhou, Q.N. Zhang, *Phys. Rev. B* 45 (1992) 10356.
- [30] M.F. Daniel, B. Desbat, J.C. Lassegues, B. Gerand, M. Figlarz, *J. Solid State Chem.* 67 (1987) 235.
- [31] V.B. Mikhailik, H. Kraus, G. Miller, M.S. Mykhaýlyk, D. Wahl, *J. Appl. Phys.* 97 (2005) 083523.
- [32] A.E. Ovechkin, V.D. Ryzhikov, G. Tamulaitis, A. Zukauskas, *Phys. Status Solidi* 103 (1987) 285.
- [33] V. Nagirnyi, E. Feldbach, L. Jönsson, M. Kirm, A. Kotlov, A. Lushchik, V.A. Nefedov, B.I. Zadneprovski, *Nucl. Instrum. Methods Phys. Res. A* 486 (2002) 395.
- [34] S. Chernov, L. Grigorjeva, D. Millers, A. Watterich, *Phys. Status Solidi B* 241 (2004) 1945.
- [35] M. Itoh, T. Katagiri, T. Aoki, M. Fujita, *Radiat. Meas.* 42 (2007) 545.
- [36] A. Kalinko, A. Kotlov, A. Kuzmin, V. Pankratov, A. I. Popov, L. Shirmane, *Centr. Eur. J. Phys.* 9 (2011) 432.